Catalysis Science & Technology

ROYAL SOCIETY OF CHEMISTRY

PAPER

View Article Online
View Journal | View Issue

Cite this: *Catal. Sci. Technol.*, 2020, 10, 4726

Dynamic structural changes of supported Pd, PdSn, and PdIn nanoparticles during continuous flow high pressure direct H_2O_2 synthesis†

Dmitry E. Doronkin, *[ab] Sheng Wang,[ac] Dmitry I. Sharapa,[a] Benedikt J. Deschner,[d] Thomas L. Sheppard,[ab] Anna Zimina,[ab] Felix Studt,[ab] Roland Dittmeyer,[d] Silke Behrens[ac] and Jan-Dierk Grunwaldt[ab]

The direct synthesis of hydrogen peroxide over TiO_2-supported mono- and bimetallic Pd, PdSn, and PdIn nanoparticles (NPs) was performed in a continuous plug-flow reactor at 80 bar in ethanol with $H_2:O_2$ ratios varied from 10:1 to 1:10. At the same time the catalysts were monitored by *operando* X-ray absorption spectroscopy (XAS). The setup optimized for XAS allowed productivities that are among the highest reported up to now. A rate of up to 580 $mmol_{H_2O_2}\ g_{cat}^{-1}\ h^{-1}$ and a H_2O_2 concentration of 80 mmol l^{-1} were obtained which were only limited by the supply of reactants. During H_2O_2 synthesis, the studied NPs revealed a face centered cubic (fcc) Pd(Sn/In) metal (alloy) structure at $H_2:O_2$ ratios equal to or smaller than 1 and the corresponding β-hydride structure at $H_2:O_2 > 1$. Under all conditions, additional SnO_2/In_2O_3 species were observed for the bimetallic catalysts. XAS supported by DFT calculations showed that alloying Pd with In or Sn limited the H_2 uptake capacity and the corresponding lattice expansion of the bimetallic NPs. Different catalysts performed best at different $H_2:O_2$ ratios. All catalysts were stable at $H_2:O_2 > 1$. Significant leaching of the active Pd and PdIn species could be observed for $H_2:O_2 \leq 1$ (quantified by XAS), while PdSn was relatively stable under these conditions. The higher stability of PdSn NPs is proposed to be due to a SnO_2 shell providing strong bonding between the NPs and the titania support.

Received 19th March 2020,
Accepted 21st June 2020

DOI: 10.1039/d0cy00553c

rsc.li/catalysis

Introduction

Hydrogen peroxide is an important environmentally friendly oxidant widely used in chemical synthesis, paper, pulp, and textile bleaching, wastewater treatment, mining, and others.[1–4] Nearly all industrially produced H_2O_2 is derived from the anthraquinone auto-oxidation[4] process introduced by Riedl and Pfleiderer.[5] This process is only economic on a large scale and produces harmful organic waste. Economy of scale brings the need for energy-intensive concentration of the H_2O_2 solution to 70 wt% at production plants, transportation of the resulting hazardous material to end users and further dilution at the end-user sites to obtain required concentrations (often <9 wt%).[3] Hence, there is a need to develop alternative processes for H_2O_2 production which are green, sustainable and economically viable on a small scale.

Direct catalytic synthesis of H_2O_2 from H_2 and O_2 is a promising reaction which allows the small-scale, decentralized production of H_2O_2 without generation of harmful byproducts.[2–4] Commercial implementation of the direct H_2O_2 synthesis is mainly hampered by safety concerns as the process requires high partial pressures, potentially forming explosive mixtures. The safety concerns hinder studies of working catalysts which limits the knowledge-based catalyst and process development. To meet the safety regulations, most of the studies on the direct catalytic H_2O_2 synthesis were performed with highly diluted gases in (semi-) batch reactors.[1,2] In addition, new and intrinsically safe

[a] *Institute of Catalysis Research and Technology, Karlsruhe Institute of Technology, Hermann-von-Helmholtz-Platz 1, Eggenstein-Leopoldshafen, 76344, Germany. E-mail: dmitry.doronkin@kit.edu*
[b] *Institute for Chemical Technology and Polymer Chemistry, Karlsruhe Institute of Technology, Engesserstr. 20, Karlsruhe, 76131, Germany*
[c] *Institute of Inorganic Chemistry, Ruprecht-Karls University Heidelberg, Im Neuenheimer Feld 270, Heidelberg, 69120, Germany*
[d] *Institute for Micro Process Engineering, Karlsruhe Institute of Technology, Hermann-von-Helmholtz-Platz 1, Eggenstein-Leopoldshafen, 76344, Germany*

† Electronic supplementary information (ESI) available: PDF describing catalyst synthesis and characterization; indirect online determination of catalytic activity and selectivity using mass spectrometry; titration of H_2O_2 with $Ce(SO_4)_2$; DFT-optimized PdSn and PdIn structures used for theoretical evaluation of hydride formation; exemplary raw k^2-weighted EXAFS data; XANES and FT EXAFS spectra of reference compounds (bulk Pd, Sn, In metals and their oxides); calculated reference XANES spectra of In^0, In_2O_3, and In-doped Pd nanoparticles; exemplary XANES and EXAFS fits; detailed results of EXAFS analysis of the experimental spectra; XAS evidence of leaching of Pd, Sn, and In species; high resolution transmission electron microscopy of used PdSn and PdIn NPs. See DOI: 10.1039/d0cy00553c

concepts, that make use of membrane reactors[6,7] and electrochemical H_2O_2 production,[3] have emerged. Recently, *operando* studies of the catalysts for H_2O_2 production were reported by eliminating the explosion hazard by using thin capillaries as *in situ* reactors[8] or dissolving H_2 and O_2 at high pressures in separate liquid streams.[9]

Platinum-group metal nanoparticles (NPs) are presently the most active catalysts for the direct H_2O_2 synthesis.[1,3] Among those supported Pd particles are often used as catalysts for the direct H_2O_2 synthesis. However, Pd also catalyses the side reactions, *i.e.* H_2O_2 decomposition or overhydrogenation to water, reducing the overall H_2O_2 selectivity. Promoting Pd with other metals, for example Au and Sn, allows improving the catalyst selectivity by suppressing these side reactions.[1,10–12] Information on the structure of bimetallic NPs and its correlation with catalytic activity and selectivity during H_2O_2 is scarce and, for the most part, obtained indirectly *via* DFT calculations, kinetic experiments and *ex situ* catalyst characterization. However, so far the structure of the bimetallic NPs producing quantitative amounts of H_2O_2 was not directly observed. In addition, catalytic testing is usually done under very limited sets of conditions, *e.g.* $H_2:O_2$ ratio often shifted to excess O_2. Previously we have reported on a setup for *operando* XAS studies of H_2O_2 synthesis catalysts in a continuous plug-flow reactor cell at high pressures and variable $H_2:O_2$ ratios. This setup unravelled the structure of Pd NPs and their hydrides during direct H_2O_2 synthesis in water at 10 bar.[9] In this work, a modified continuous flow setup is used to provide direct information on the structure, dynamics, activity and selectivity of supported monometallic Pd and bimetallic PdSn and PdIn NPs, including formation of hydrides. All data are obtained during the direct catalytic synthesis of H_2O_2 at 80 bar in ethanol while the feed composition was varied in a wide range from high H_2 excess to high O_2 excess. The data are used to provide structure–activity correlations, define catalyst stability regions and outline the most promising operating conditions for the subsequent process optimization.

Materials and methods

Catalyst synthesis

Mono- and bimetallic catalysts were synthesized by depositing Pd(M) nanoparticles on TiO_2 (Aeroxide® P25) pre-treated with diluted H_2SO_4 (denoted as s-TiO_2) as reported previously[13,14] to obtain Pd/s-TiO_2 (4.5 wt% Pd); PdSn/s-TiO_2 (4.1 wt% Pd and 2.8 wt% Sn); PdIn/s-TiO_2 (3.4 wt% Pd and 1.2 wt% In) catalysts. For convenience, the synthesis procedure is summarized in the ESI.† Detailed characterisation (TEM, EDX mapping, XRD, XAS) of the isolated unsupported bimetallic nanoparticles and the supported catalysts is reported in our recent publication.[14] TEM analysis reported in the cited work[14] reveals relatively broad NP size distribution between 2 and 6 nm with maxima at 3–4 nm.

Operando setup and experimental test procedure

The experimental setup used in this study is based on the concept described by us earlier.[9] Essentially, in order to avoid mixing O_2 and H_2 in the gas phase, they are dissolved in separate solvent streams and the obtained liquid H_2 and O_2 solutions are mixed before the *in situ* cell. A scheme of the setup and a photo of the stainless steel liquid flow *in situ* cell used as a catalytic reactor are given in Fig. 1. The setup and the cell are built of stainless steel passivated with 30 wt% HNO_3 according to ref. 15 with 2 mm thick polyether ether ketone (PEEK) X-ray windows. Two HPLC pumps pump the acidic ethanol (Normapur, denatured with 1 wt% methyl ethyl ketone, MEK, with 0.12 M H_2SO_4, and a trace amount of 0.3 ± 0.03 wt% water) from separate containers flushed with technical N_2. In a separate experiment the catalytic activity in ethanol denatured with MEK was found to be comparable to the activity observed in absolute ethanol. Due to high consumption of ethanol during catalytic experiments and cost reasons, denatured ethanol was used for the *operando* measurements. The solvent streams were then mixed with H_2 or O_2 gas streams in SiC-packed columns at high pressure to allow complete dissolution of the respective gases. The obtained liquid solutions were mixed together, flown through the *in situ* cell, and depressurized after a back pressure regulator (BPR) into a product container flushed with N_2 at 280 ml min^{-1}. The flushing gas containing unreacted H_2 and O_2 was eventually sampled by a quadrupole mass spectrometer (MS, Pfeiffer Vacuum OmniStar GSD 320).

The setup was operated at 296 K (ambient temperature) and 80 (±2) bar. 25 mg of pressed and sieved catalyst (sieve fraction 80–160 μm) was used resulting in a catalyst bed volume of 4 (±0.5) mm (length) × 5 mm (depth defining the X-ray path length) × 1 mm (height). The catalyst was packed between two quartz wool plugs and supported on both sides by 6–8 mm long SiC packed beds for better stability. Combined liquid flow was 3 ml min^{-1} resulting in the liquid hourly space velocity (LHSV) 9000 h^{-1} and the residence time in the catalyst bed 0.4 s. For the measurements at different $H_2:O_2$ ratios the liquid flows were kept constant and the gas flows were varied.

Note that the experiment is potentially dangerous and can be operated only with pressure-rated equipment and after appropriate testing. Protection measures should include nitrogen purge, overpressure protection of the HPLC pumps and/or pressure relief valves as well as tubing and cells with small volume and openings (max. 1–2 mm) which would act as flame arrestors.[16] Parts (especially, MFC and shut-off valves) that are in direct contact with gaseous oxygen at high pressure require special cleaning (grease-free).

The liquid and gas flows used are listed in Table 1 in the same order as the measurements were performed. For each set of conditions, after changing the gas flows, a waiting time of approx. 60–80 minutes (or until stable MS readings were obtained) was allowed before starting XAS measurements. The exact timings of each experiment are discussed in the section

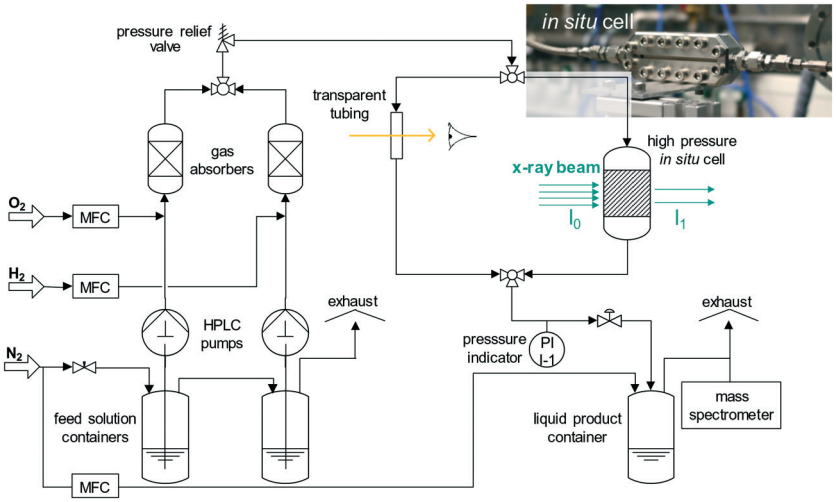

Fig. 1 Scheme of the experimental setup for *operando* studies of the direct H_2O_2 synthesis and a photo of the reactor (*in situ* cell, top right).

Table 1 Reaction conditions during *operando* XAS measurements listed in the same order as they were performed. Flows are given in ml_{STP} min^{-1} (calibrated at 273.15 K and 1013.25 hPa)

$H_2:O_2$ ratio	H_2 gas flow [ml min^{-1}]	Liquid flow (H_2 channel) [ml min^{-1}]	O_2 gas flow [ml min^{-1}]	Liquid flow (O_2 channel) [ml min^{-1}]
H_2 only	10	1.5	0	1.5
10 : 1	10	1.5	1	1.5
3 : 1	10	1.5	3.33	1.5
1 : 1	10	1.5	10	1.5
1 : 3	3.33	1.5	10	1.5
1 : 10	1	1.5	10	1.5
O_2 only	0	1.5	10	1.5
3 : 2[a]	10	1.5	6.67	1.5

[a] This step was performed only during the PdIn catalyst test.

"Leaching of Pd, Sn, and In during synthesis of H_2O_2" in which longer gaps between the measurements were due to two reasons: (a) waiting for injection of electrons in the synchrotron storage ring (PdSn/s-TiO_2 and Pd/s-TiO_2 at 4–6 h time on stream, TOS), and (b) due to continuously changing concentrations of the H_2 and O_2 at the outlet (Pd/s-TiO_2 at 10–12 h TOS and PdIn/s-TiO_2 at 8–13 and 14–17 TOS). The order in which measurements were performed was defined by the fact that less time is needed to stabilize reactant and product concentrations at higher $H_2:O_2$ ratios which, as will be shown in the discussion, directly affects catalyst stability. This stepwise change from stabilizing to leaching conditions made it possible to use one catalyst loading per each catalyst sample. At the end of the study reversibility of the catalyst structure and operation was checked by returning the leached PdIn/s-TiO_2 catalyst sharply from oxidizing conditions back to reducing $H_2:O_2$ ratio of 3 : 2.

After stabilization of H_2 and O_2 outlet concentrations the product container was replaced with a clean and dry one and the product solution was collected while the XAS measurements were performed. XAS spectra were recorded once near the inlet (probing the zone at 0.5–1.5 mm from the inlet) and once near the outlet (probing the zone at 2.5–3.5 mm out of 4 from the inlet) of the catalyst bed at Pd–K and, if applicable, at Sn–K/In–K edges. Each spectrum measurement took approx. 30 min.

H_2O_2 yield and selectivity were monitored and quantified in several ways. Indirect online monitoring was based on the negligible solubility of H_2 and O_2 at ambient pressure which led to separation of unreacted H_2 and O_2 from the liquid solution after depressurization and allowed their semi-quantitative (±10% relative error) quantification using the MS, the detailed procedure and results are provided in the ESI.† This quantification for $H_2:O_2$ ratios between 3 : 1 and 1 : 3 yielded results in a good agreement with results obtained by titration of H_2O_2 (ESI,† Table S1).

Precise evaluation of the H_2O_2 yields was done *via* titration of the product solution. Titration was performed immediately after the respective experiment whenever possible, otherwise product solutions were stored in glass vials in a dark cold (−27 °C) environment to ensure no H_2O_2 decomposition before titration. To ensure reproducibility of the results, product solutions were titrated independently using two different methods. H_2O_2 concentration reported in the main text was obtained *via* reaction with a $TiOSO_4/H_2SO_4$ reagent after which the absorption of the formed complex was

analysed using a UV-vis spectrophotometer (Specord S600, Analytik Jena).[17] H_2O_2 in the obtained product solution was also titrated with $Ce(SO_4)_2$ (*cf.* experimental details and results in the ESI†).[18]

The amount of water in the product solution was determined by Karl Fischer (KF) titration[19] on a Metrohm Titrando 841 titrator using HYDRANAL-Methanol dry and HYDRANAL-Composite 5 (Sigma Aldrich) as a solvent and a reagent for the titration, respectively. H_2O_2 yield and selectivity to H_2O_2 were calculated from concentrations of H_2 and O_2 dissolved in the feed solution as well as produced H_2O and H_2O_2 concentrations determined by titration as:

$$Y_{H_2O_2} = \frac{C_{H_2O_2}}{\min(C_{H_2}, C_{O_2})}, \quad (1)$$

$$S_{H_2O_2} = \frac{C_{H_2O_2}}{C_{H_2O_2} + C_{H_2O}}. \quad (2)$$

X-ray absorption spectroscopy and data analysis

The XAS measurements at Pd–K, Sn–K, and In–K absorption edges (24 350 eV, 29 200 eV, and 27 940 eV, correspondently) were performed at the CAT-ACT beamline of the KIT synchrotron (Karlsruhe, Germany).[20] The CAT experimental station was designed for *operando* studies of heterogeneous catalysts and has the necessary infrastructure for catalytic experiments including high pressure gas dosing infrastructure and analytics.[20] Before the beamtime the experiment was set up and thoroughly tested without X-ray beam.

X-rays were generated using a 2.5 T wiggler source (40 poles, 48 mm period length) and the photon energy was selected with a double crystal monochromator with a Si (311) crystal pair. Higher harmonics rejection was performed using Rh-coated mirrors. Energy was calibrated using spectra of reference Pd/Sn/In metal foils measured simultaneously with spectra of the catalysts. The beam size was 0.9 mm (vert.) × 1 mm (hor.). The experiments were performed in transmission geometry using the nominal high energy ionization chambers to determine the X-ray intensity before the sample, after the sample, and after the reference metal foil.

The spectra were normalized and the extended X-ray absorption fine structure (EXAFS) spectra were background subtracted using the ATHENA program from the IFEFFIT software package.[21] k^1-, k^2-, and k^3-weighted EXAFS functions were Fourier transformed in the k range of 2.5–12.5 $Å^{-1}$ (Pd–K edge), 2.0–13.0 $Å^{-1}$ (Sn–K edge), and 2.0–10.5 $Å^{-1}$ (In–K edge) and multiplied by a Hanning window function with sill size of 1 $Å^{-1}$. The structural model for fitting the Pd–K edge spectra was based on the Pd metal structure (ICSD collection code 52251). The model for fitting the In–K edge spectra was based on a mixture of the first In–O shell from the In_2O_3 crystal structure (ICSD collection code 14387) and the first In–Pd shell from the model of the Pd metal structure with In as a central atom (fits using pure In metal structure as a model were unsuccessful). The corresponding theoretical backscattering amplitudes and phases were calculated by FEFF 6.0.[22] Structure refinement was performed using ARTEMIS software (IFEFFIT).[21] The theoretical data were then adjusted to the experimental spectra by the least square method in R-space between 1.2 and 3 Å (Pd–K spectra) or 1.0 and 3 Å (In–K spectra). First, the amplitude reduction factors (S_0^2 = 0.78 for Pd and S_0^2 = 0.75 for In) were calculated from the fits of reference spectra of Pd and In foils and then the coordination numbers, interatomic distances, energy shift (δE_0) and mean square deviation of interatomic distances (σ^2) were refined. The absolute misfit between theory and experiment was expressed by ρ.[21] Pd, Sn, and In nearest neighbors could not be distinguished in the fits due to similar scattering factors.

Density functional theory calculations

DFT calculations were performed using the VASP package (version 5.4.1).[23] The bulk alloys were modelled with a 2 × 2 × 2 supercell (corresponding to 32 metal atoms in one unit cell). The structures were fully optimized with respect to the position of atoms, the cell volume, and the cell shape. PdSn and PdIn alloys were modelled with 4 Pd atoms in the supercell being exchanged with In or Sn (corresponding to a 12.5 at% doping). An energy cutoff of 450 eV was used as negligible change of the lattice constant was observed for higher cutoffs (see Fig. S1†) (compare to ref. 24) and a k-point sampling of 6 × 6 × 6 was used. Two independent sets of calculations with different GGA-functionals were performed for each system: the BEEF-vdW,[25] that is known to provide accurate adsorption energies and reaction barriers on transition metal surfaces,[26,27] was used to calculate the reaction energies, while PBE-sol,[28] a functional known to provide accurate bulk parameters, was used to calculate interatomic distances.

In the first step an optimal distribution of In and Sn dopants in Pd metal was computed. Among the six starting distributions five that had no neighbouring dopant atoms (no short In–In or Sn–Sn contacts) were found to have low differences in energy, while the one with tetrahedral dopant clusters appears to be energetically unfavourable (In–In repulsion significantly distorts the crystal structure). This agrees with the fact that Pd–In and Pd–Sn alloys are known not to contain any clusters of dopant atoms or any short In–In or Sn–Sn contacts.[29–31] For further investigation, structures with the most distant dopant atoms were chosen (see ESI†).

Transmission electron microscopy

For transmission electron microscopy (TEM), the samples were deposited in dry state on Cu grids covered with holey carbon film. The samples were examined in an FEI Titan 80-300 aberration corrected electron microscope operated at 300 kV. Scanning transmission electron microscopy (STEM) images were acquired using a Fischione model 3000 HAADF (high-angle annular dark-field) STEM detector and energy dispersive X-ray spectra (EDX) were acquired using an EDAX SUTW EDX

detector. TEM images were evaluated using ImageJ.[32] Particle size was estimated as an average of minor and major axes of an ellipse enclosing the corresponding particle.

Results and discussion

Activity and selectivity to H_2O_2 measured during spectroscopic study

The catalytic data on the three tested catalysts measured during *operando* XAS experiments are summarized in Fig. 2. H_2O_2 concentrations obtained by $TiOSO_4$ photometric determination (Fig. 2a, c and e) agree with those obtained by $Ce(SO_4)_2$ titration (with a systematic discrepancy of approx. 10%, Table S1†) and qualitatively agree with the results of online MS monitoring (Table S1†). Due to the experiment design in which the space velocity was kept the same but the amount of dissolved gases was decreased to obtain different $H_2:O_2$ ratios, the maximum achievable H_2O_2 concentrations were also different (red circles in Fig. 2a, c and e). The monometallic Pd catalyst (Pd/s-TiO_2) showed rather high

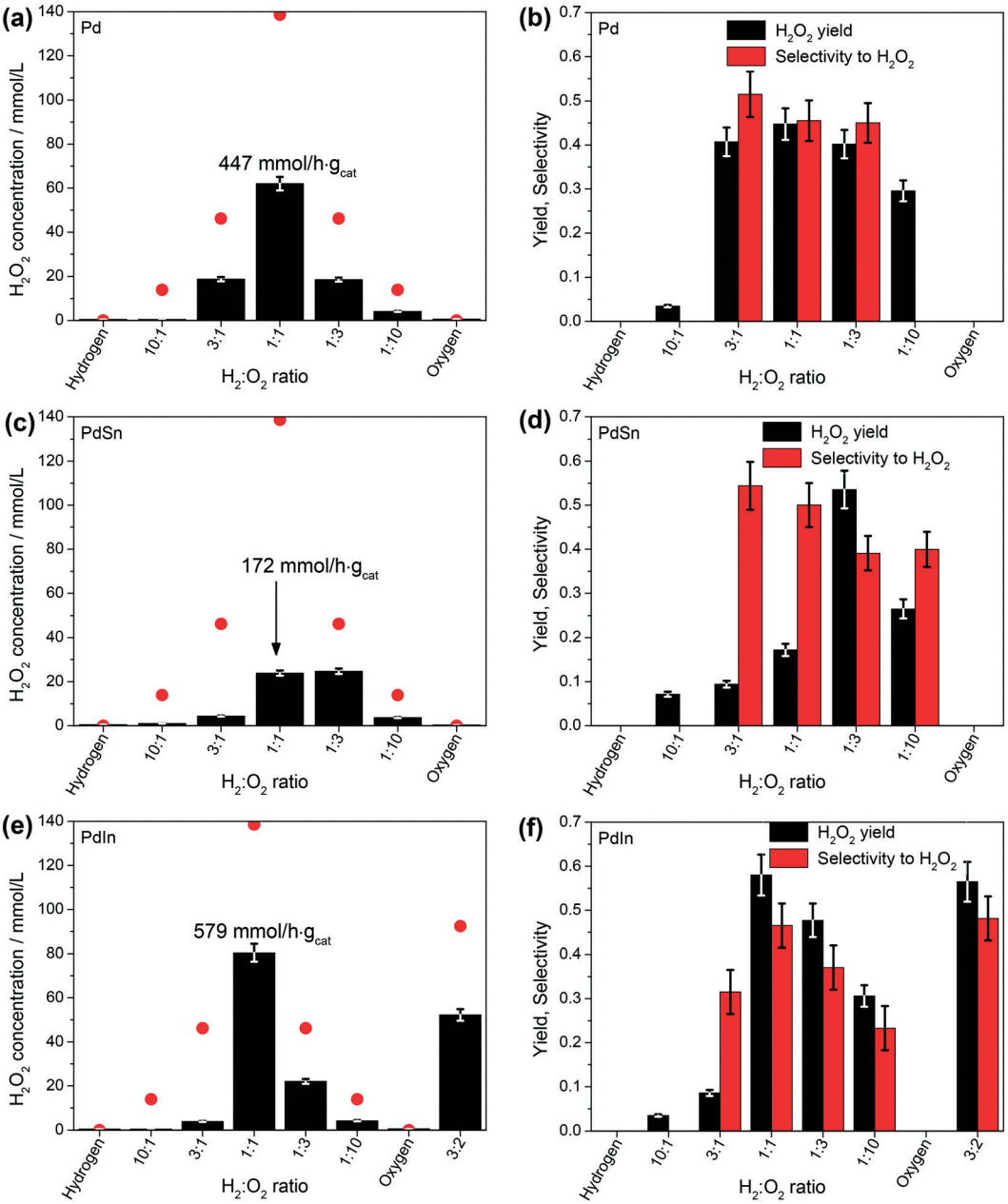

Fig. 2 (a, c and e): Theoretically achievable (red circles) and experimentally determined (black bars) H_2O_2 concentrations together with achieved H_2O_2 production rates at $H_2:O_2 = 1:1$. (b, d and f): H_2O_2 yields and selectivities observed during *operando* XAS measurements. H_2O_2 and H_2O concentrations presented here were obtained by photometric titration with $TiOSO_4$ and Karl Fischer titration, respectively, for the online MS and $Ce(SO_4)_2$ titration data see Table S1.†

H_2O_2 yields and selectivities, both in the range of approx. 40–50%, implying full conversion of the limiting reactant at $H_2:O_2$ ratios between 3 : 1 and 1 : 3 (*cf.* Table S1† for conversions of H_2 and O_2 obtained from MS data). The Pd catalyst showed similar H_2O_2 yields and selectivities at $H_2:O_2$ = 3 : 1–1 : 3, independent of the exact $H_2:O_2$ ratio. Doping Pd with Sn and In in PdSn ($PdSn/s\text{-}TiO_2$) and PdIn ($PdIn/s\text{-}TiO_2$) catalysts significantly altered the catalytic behaviour of the resulting catalysts. Compared to Pd, the catalytic activity was drastically decreased under hydrogen excess (Fig. 2b, d and f). Approaching stoichiometric and oxygen-rich conditions led to an improvement in H_2O_2 yields over PdIn (very active already at $H_2:O_2$ = 1 : 1) and PdSn which showed H_2O_2 yields above 50% only in excess of oxygen ($H_2:O_2$ = 1 : 3). Under oxygen-rich conditions productivity of all three catalysts was similar.

The high activity of the catalyst means that the maximum H_2O_2 productivity was limited by the availability of reactants and could be achieved at $H_2:O_2$ ratio 1 : 1 (as the maximum amount of the gases was dosed in this experiment) for $Pd/s\text{-}TiO_2$ and $PdIn/s\text{-}TiO_2$. This does not allow determination of the specific activity of the catalysts, instead only a lower limit on the H_2O_2 productivities could be identified as 447 $mmol_{H_2O_2}\ g_{cat}^{-1}\ h^{-1}$ and 579 $mmol_{H_2O_2}\ g_{cat}^{-1}\ h^{-1}$ for $Pd/s\text{-}TiO_2$ and $PdIn/s\text{-}TiO_2$ catalysts, respectively. The highest obtained H_2O_2 concentration was 80 mmol L^{-1} or approx. 0.3 wt%.

Although the setup was optimized for spectroscopy, the obtained productivities are, to our knowledge, among the highest published in the literature. They are at least three times higher than productivities obtained in (semi-)batch reactors as reviewed by Edwards *et al.*[1] and only two times lower than productivities reported by Gudarzi *et al.*[33] over Pd and PdAu supported on activated carbon cloth. Since in our case H_2O_2 production rates were limited not by kinetics but by the concentrations of dissolved gases (max. 139 mmol L^{-1} for each of H_2 and O_2), optimization of the reaction parameters (contact time, pressure and amount of dissolved gases) could further increase the H_2O_2 production rates.

Operando X-ray absorption spectroscopy

XAS spectra in terms of XANES and EXAFS were measured in a spatially defined way near the inlet and near the outlet of the catalyst bed in each *operando* experiment. In all cases the Pd–K edge spectra measured in the same experiment were similar and, therefore no gradients in speciation were evident along the catalyst bed. Therefore, only one set of spectra measured near the inlet of the catalyst bed will be shown and discussed. Fig. 3 shows *operando* XANES and Fourier transformed (FT) k^2-weighted EXAFS spectra of the three catalyst samples measured at the Pd–K edge under all test conditions. Fig. S2 (ESI†) shows the k^2-weighted EXAFS data to allow evaluating the raw data quality. Qualitatively, all recorded Pd–K edge spectra show the same features as the Pd metal spectrum (Fig. S3†), independently on the experimental conditions or catalyst composition (monometallic Pd and bimetallic PdSn and PdIn).

Hence, in all cases Pd species are composed of Pd NPs. No spectral features attributed to either PdO phase (high backscattering on O or Pd at uncorrected distances of 1.5 and 3 Å, correspondingly, in FT EXAFS, Fig. S3†) or chemisorbed oxygen species on the Pd NP surface (higher white line and a peak at 24 375 eV in XANES) could be observed in any of the experimental Pd–K edge spectra in this work, even under excess O_2. This is different to our previous observations on the H_2O_2 synthesis over Pd/TiO_2 in water where surface chemisorbed oxygen species could be identified in the *operando* spectra.[9] The difference is attributed to the effect of ethanol solvent which provides net reducing environment since it is a dominating reagent in the system, even if O_2 is dissolved. Full reduction of Pd NPs in alcohols was evidenced previously by Grunwaldt *et al.*[34] and, in relation to H_2O_2 synthesis in methanol, also by Kanungo *et al.*[8] While surface chemisorbed O was visible in aqueous solution,[9] the same Pd NPs were fully reduced in a separate experiment with pure ethanol (even containing dissolved O_2).[35] The other contributing factor, as compared to our previous study,[9] is that NPs of larger size were used in this work which results in a very small fraction of surface Pd (<1%)[36] (almost invisible for conventional XAS) and could further explain the inability to observe surface oxygen in this study. Furthermore, it was demonstrated that larger (>4 nm) Pd NPs reduce easier than NPs with sizes below 2 nm.[37,38]

The observed spectral features shifted with changing $H_2:O_2$ ratio between H_2-rich and O_2-rich feeds (Fig. 3). Two descriptors were used to evaluate the spectral changes, one for XANES (position of the 2nd peak above the absorption edge, predominantly, reflecting changes in the electronic structure of Pd), and one for EXAFS (average Pd–Pd(In,Sn) bond distance reflecting local structural changes around Pd atoms). Exemplary Pd–K EXAFS fits are provided in the ESI,† Fig. S6 and the detailed fitting parameters are listed in the Tables S3–S5.† In the H_2 only feed and at $H_2:O_2$ ratios 10 : 1 and 3 : 1 the XANES maxima shift to lower energies while EXAFS shows backscattering at a larger distance (Fig. 3). Such changes in the XANES and EXAFS spectra of Pd NPs under excess H_2 were observed by us in the previous work[9] and attributed to the formation of Pd hydride.[34,39–41] The two clearly separated groups of spectra (in H_2 excess and O_2 excess) of $Pd/s\text{-}TiO_2$ and $PdIn/s\text{-}TiO_2$ catalysts reveal evident structure expansion (β-hydride formation) while the spectra of $PdSn/s\text{-}TiO_2$ measured in H_2 excess and O_2 excess differ less clearly from each other and require further analysis to identify structural changes.

To identify the state of the second metal in the $PdSn/s\text{-}TiO_2$ and $PdIn/s\text{-}TiO_2$ catalysts, the corresponding Sn–K edge and In–K edge *operando* XAS spectra were recorded (Fig. 4, raw EXAFS data in Fig. S2†). Sn–K edge XANES spectra are similar to the SnO_2 reference spectrum (Fig. S4†). This similarity is further supported by FT EXAFS data with only the first shell at 1.5 Å (not corrected for the phase shift)

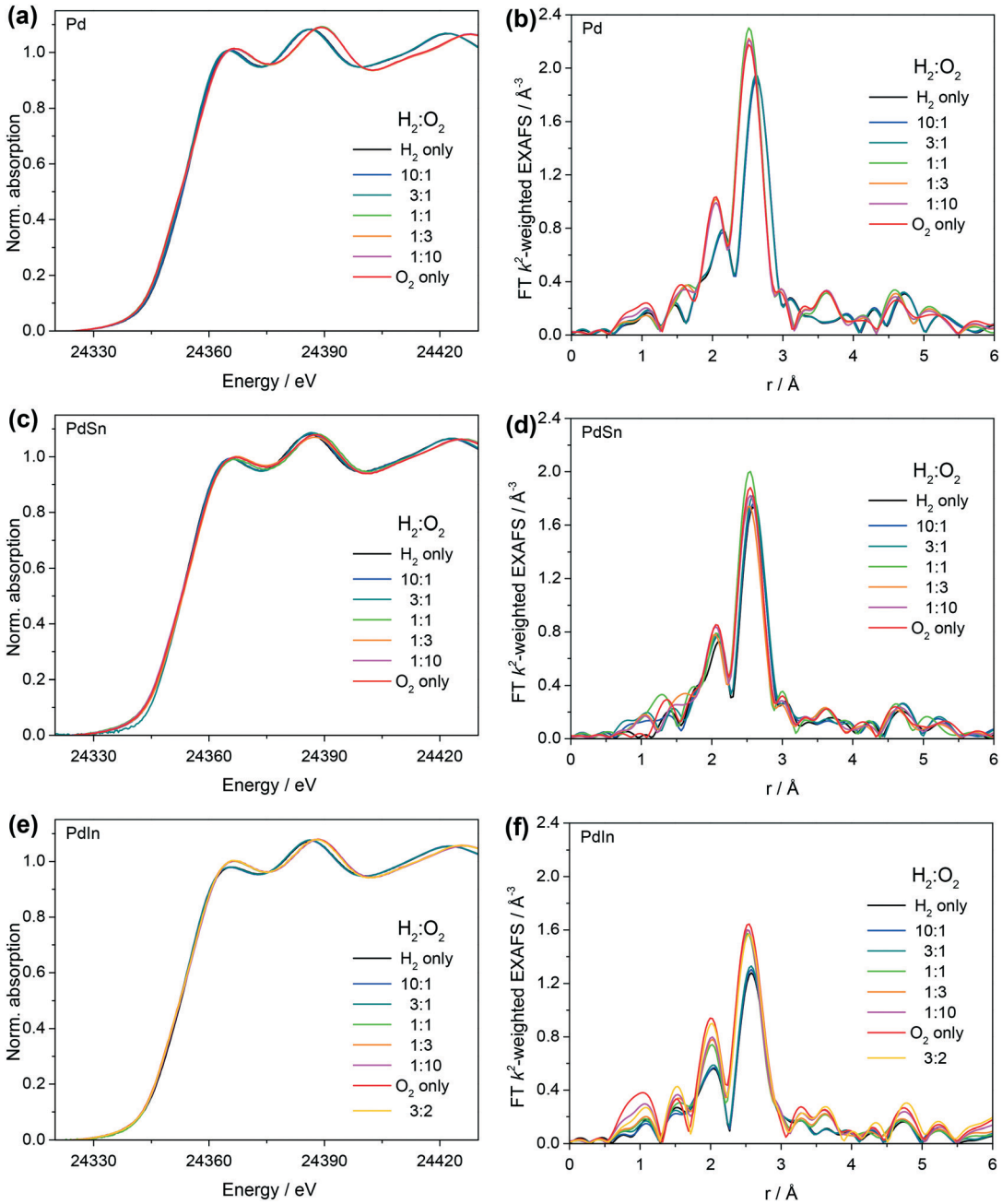

Fig. 3 *Operando* XANES and FT k^2-weighted EXAFS (uncorrected for the phase shift) measured at Pd–K absorption edge during direct synthesis of H_2O_2 at 80 bar over (a and b) Pd/s-TiO_2, (c and d) PdSn/s-TiO_2, and (e and f) PdIn/s-TiO_2 catalysts. Catalytic properties are reported in Fig. 2.

visible corresponding to O neighbours. Noteworthy, no second shell is found in the EXAFS of PdSn/s-TiO_2 compared to the SnO_2 spectrum (Fig. S4†), hence, the majority of the observed SnO_x species in the PdSn/s-TiO_2 are highly disordered. As shown in the previous work,[14] during the metal deposition both Pd and Sn were kept in tight contact as PdSn nanoparticles, hence we suppose that, in lieu of high temperature pretreatment, SnO_x species are still in tight contact with Pd, possibly as a thin layer covering Pd NPs.[11] With respect to the dynamics of Sn species in the PdSn/s-TiO_2, the intensity of the XANES white line (peak at 29 210 eV) slightly lowers under H_2 excess suggesting reversible reduction of a small fraction of SnO_x species. The fraction of Sn^{4+} was determined using linear combination analysis (LCA) of the *operando* XANES spectra in the range 29 185–29 235 eV using Sn–K edge spectra of Sn^0 and SnO_2 as references (Fig. 5a). Exemplary LCA XANES fits at the Sn–K edge are given in Fig. S7.† At the start of the experiment (under H_2 excess) approx. 30% of Sn species are reduced whereas under O_2 excess this number decreases to approx. 22%. The obtained absolute numbers should be taken with caution as the reference spectra do not perfectly

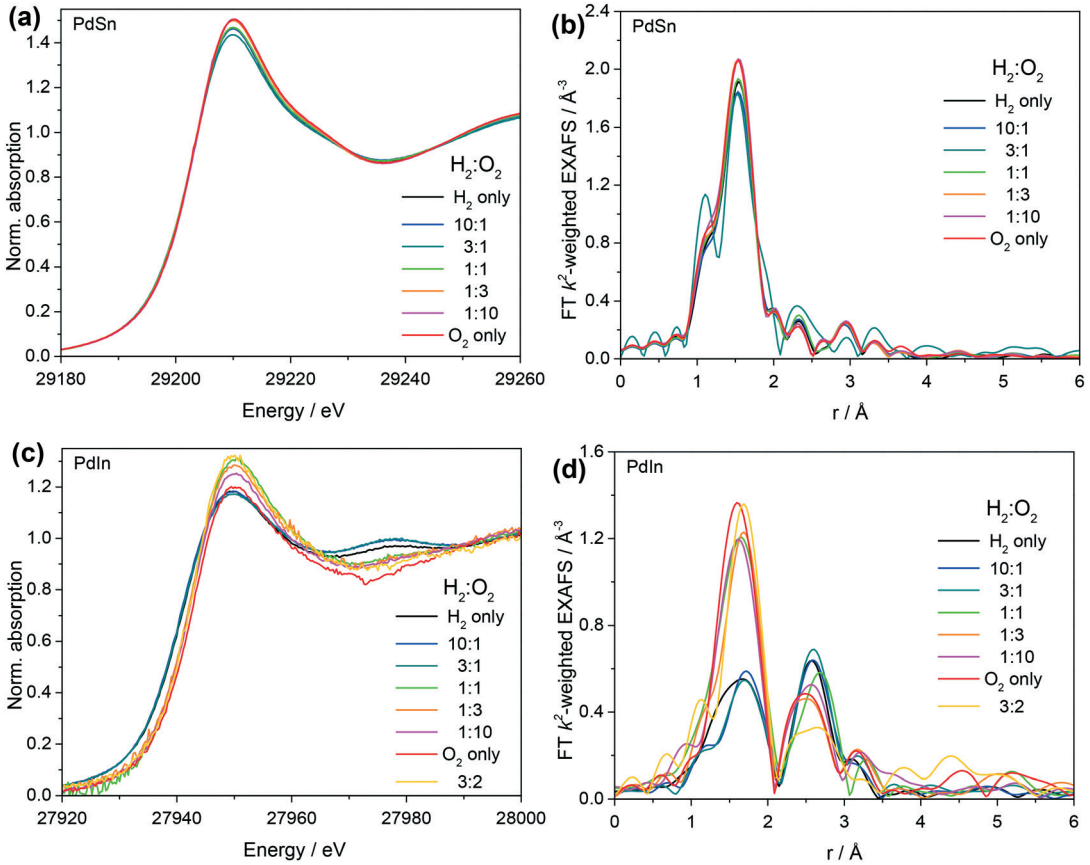

Fig. 4 *Operando* XANES and FT k^2-weighted EXAFS (uncorrected for the phase shift) measured at (a and b) Sn–K and (c and d) In–K absorption edges during direct synthesis of H_2O_2 at 80 bar over (a and b) PdSn/s-TiO_2 and (c and d) PdIn/s-TiO_2. Catalytic properties are reported in Fig. 2.

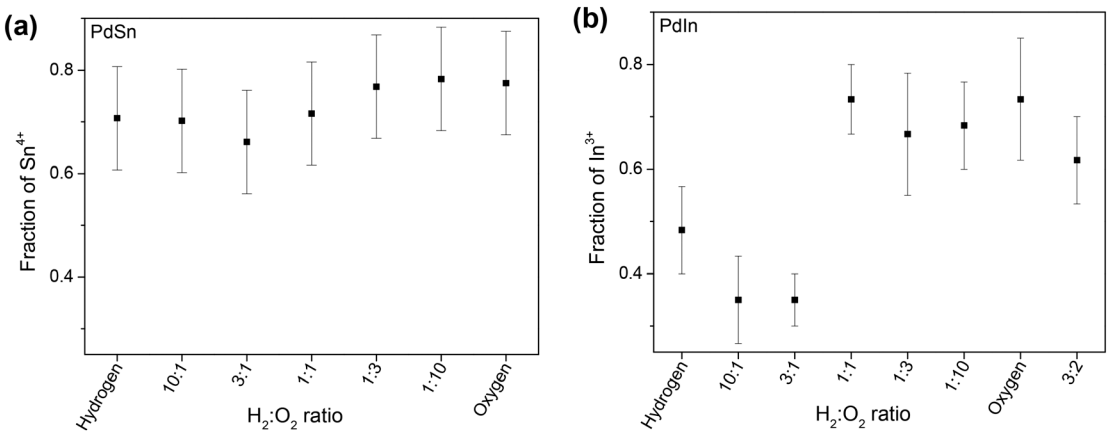

Fig. 5 Molar fractions of Sn^{4+} (in the Sn^0–SnO_2 mixture) and In^{3+} species (in the PdIn^0–In_2O_3 mixture) obtained from (a) linear combination analysis of *operando* Sn–K XANES and (b) coordination number of (O) in the first shell around In obtained from In–K edge EXAFS spectra measured during direct synthesis of H_2O_2 at 80 bar over (a) PdSn/s-TiO_2 and (b) PdIn/s-TiO_2.

reproduce the pure states seen in the particular catalyst and this is reflected in the corresponding error bars, however the trends are reliable due to low noise in the original data (Fig. 4a).

Unlike the Sn–K spectra, *operando* XANES and FT EXAFS spectra of the PdIn/s-TiO_2 measured at the In–K edge (Fig. 4c and d) change significantly with $H_2:O_2$ ratio. XANES spectra measured under O_2 excess reveal features (white line peak at 27 950 eV and a valley with a minimum at 27 975 eV) characteristic for In_2O_3 oxide (Fig. S5†). The spectra change under H_2 excess (Fig. 4c), the absorption edge shifts to lower energies, the white line intensity decreases, and a new peak

at 27 980 eV appears. The absorption edge shift and decreased white line intensity are typical signs of reduction of transition metals, however, the In–K edge spectra under H_2 excess are markedly different from the metallic In spectrum (Fig. S5†). Therefore, the reduced In species cannot be assigned to pure In NPs. An alternative model for In species is In-doped Pd NPs. The corresponding theoretical XANES spectrum of this species was calculated and indeed shows features (most importantly, the peak at approx. 2975 eV which is not present in either In_2O_3 or metallic In reference spectra) similar to the ones in the experimental spectra (Fig. S8†). The same structural model is received from the detailed analysis of the EXAFS spectra (Table S2†). Two backscattering peaks at 1.6 Å and 2.6 Å (not corrected for the phase shift) can be distinguished in the In–K edge *operando* FT EXAFS spectra (Fig. 4d). The peak at 1.6 Å can be attributed to backscattering on the first shell composed of oxygen neighbours (similar to In_2O_3, Fig. S5†), the intensity of this peak decreases if more H_2 is present in the feed. The second peak at 2.6 Å, intensity of which increases under H_2 excess, cannot be attributed to In–In interaction in metallic In (approx. 3.0 Å) or in In_2O_3 (3.3 Å, Fig. S5†). However, it corresponds to the Pd–Pd interaction in the metallic Pd lattice (Fig. S3†). In fact, assuming an In-doped Pd lattice as a structural model leads to good fit results (Table S2†). Hence, the In–K edge spectra confirm that a fraction of In atoms forms PdIn alloy while the rest form In oxide species. Due to the lack of reference XANES spectra of a well-defined PdIn alloy, LCA of XANES spectra cannot be used to quantify the oxidation state of In. Instead, coordination numbers in the first shell (CN(O), Table S2,† exemplary EXAFS fits in Fig. S7†) are used to evaluate the In^0 fraction in a mixture with In^{3+} assuming octahedral coordination of In^{3+} in oxidic species (Fig. 5b). Because of the very slow reduction, the first experimental spectrum measured in H_2 only feed shows higher In oxidation state than in the spectra taken later. Compared to the oxidation state of Sn, the fraction of reduced In during H_2O_2 synthesis is with 65% In^0 in excess H_2 much higher. Under excess O_2 the fraction of reduced In decreases to 25–30% which is comparable with the SnO_2 fraction in the PdSn sample. Due to statistical uncertainties in the coordination number determination from EXAFS, the absolute error bars resulting from such an analysis are high.

Coordination numbers in the first shell around metallic In sites (Table S2†) corrected by the fraction of metallic In (Fig. 5b) correspond to the coordination numbers around Pd atoms in the PdIn/s-TiO_2 catalyst (Table S5†) confirming random bulk alloy structure.

Structure of Pd, PdSn, and PdIn hydride species determined by *operando* XAS

PdH_x formation and stoichiometry reveals itself in the Pd–K edge XANES and EXAFS spectra in numerous ways. The most straightforward way to detect interstitial hydride is by determining the Pd lattice expansion by X-ray diffraction[42] or elongation of Pd–Pd bonds in EXAFS.[9,39,40,43] This direct proof, however, allows detecting only β-PdH_x. In case of formation of the intermediate α-PdH_x phase and the corresponding very small lattice expansion EXAFS is not sensitive enough but XANES may be used. Both α-PdH_x and β-PdH_x can be detected *via* shifts of the rising edge position and the XANES peak positions (due to core-hole shielding effect).[40] An increase in the Debye–Waller factor due to inhomogeneous H distribution in Pd nanoparticles and the resulting broader distribution of Pd–Pd interatomic distances can also indirectly prove the formation of α-PdH_x and β-PdH_x hydrides.[43–46]

The structural parameters could be extracted by fitting the *operando* Pd–K edge EXAFS spectra of Pd/s-TiO_2, PdSn/s-TiO_2, and PdIn/s-TiO_2 catalysts. The fit results are summarized in Tables S3–S5.† All mentioned structural parameters for all three studied catalysts abruptly change when H_2-rich conditions change to stoichiometric $H_2:O_2$ ratio = 1 : 1 and O_2-rich feed indicating decomposition of β-Pd(Sn, In)H_x NPs (Fig. 6a–c). Since EXAFS shows only weak sensitivity to α-PdH_x, the XANES data need to be analysed as well. Fig. 6 shows the interatomic distances as the most important structural descriptor obtained from EXAFS (showing β-hydride formation) along with the position of the 2nd peak in the *operando* XANES spectra (showing both α- and β-hydride). In all three catalysts both EXAFS and XANES spectra measured at Pd–K edge change at the same time during switch of the $H_2:O_2$ ratio from 3 : 1 to 1 : 1. This simultaneous change of both EXAFS and XANES spectra implies decomposition of β-Pd(Sn,In)H_x hydrides directly to metallic Pd(Sn,In) NPs without an intermediate α-hydride phase. This result is markedly different from our previous study of Pd NPs at lower partial pressures in water[9] and ethanol[35] where α-PdH_x was observed in the catalyst producing H_2O_2. The difference may originate from a much higher concentration of H_2 and O_2 in the liquid feed, higher pressure, different catalyst with larger more uniform Pd(Sn, In) NPs (which form β-hydrides under milder conditions and in this way may influence also the catalytic properties)[47] and a different, acid-pretreated, support.

Although the catalysts display similar structural dynamics during H_2O_2 synthesis, Fig. 6 also highlights important differences between the structure of monometallic Pd and structures of bimetallic PdSn and PdIn NPs. The EXAFS and XANES data (known to be highly sensitive to the crystal structure type[48,49]) with features matching the Pd reference spectrum (Fig. S3†) confirm the fcc Pd lattice structure in all three catalysts. However, average interatomic distances and structure expansion factors are different in all three cases. The Pd–Pd distance in the monometallic Pd NPs was calculated to be 2.739 (±0.008) Å and it increased to 2.836 (±0.004) Å under H_2 excess as a result of β-PdH_x formation (Table S3, exemplary fits in Fig. S6†). On the other hand, the minimal observed Pd–M (where M can be Pd, Sn, or In) distances in bimetallic PdSn and PdIn NPs in non-hydride state were longer than in monometallic Pd NPs at approx.

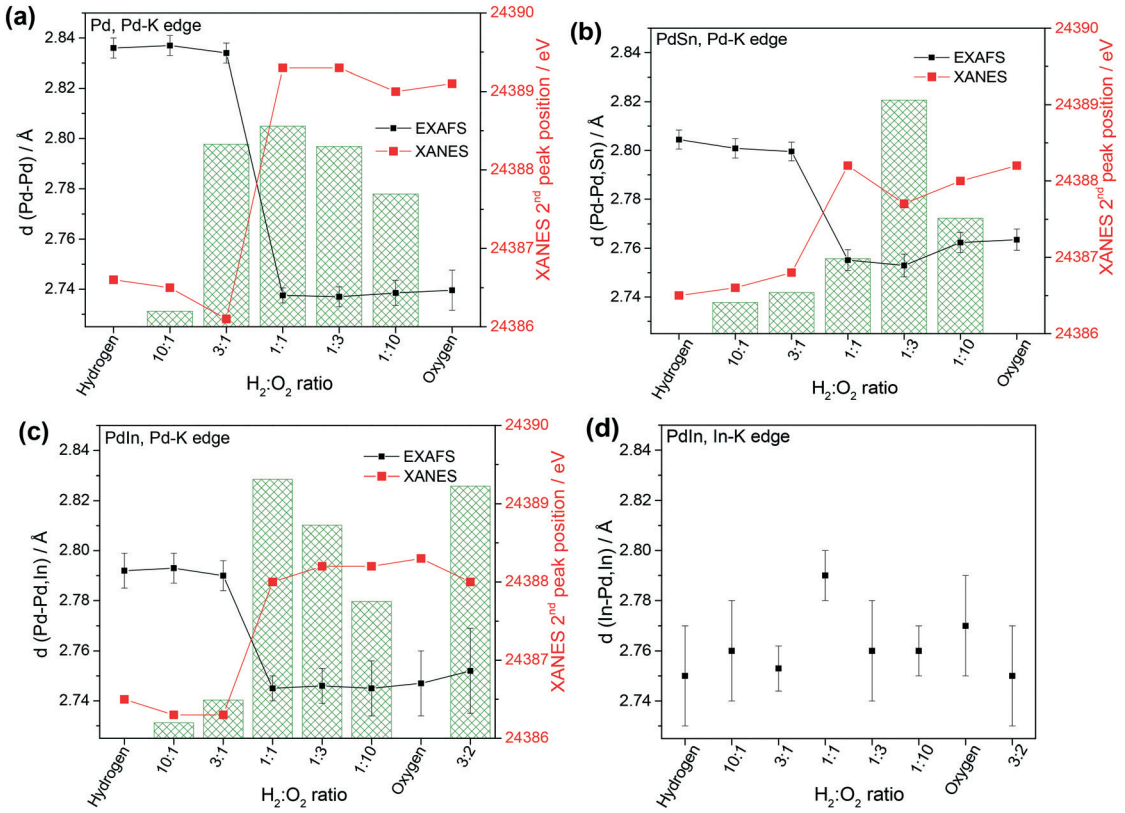

Fig. 6 Pd–Pd(Sn,In) and In–Pd(In) interatomic distances obtained from analysis of *operando* Pd–K and In–K edge EXAFS and position of the 2nd peak after absorption maximum in the *operando* Pd–K edge XANES spectra obtained during direct synthesis of H_2O_2 at 80 bar over (a) Pd/s-TiO_2, (b) PdSn/s-TiO_2, and (c and d) PdIn/s-TiO_2 catalysts. Lines connecting the data points serve as guides to the eye. Hatch patterns serve to illustrate the trends in H_2O_2 yields reported in Fig. 2.

2.753 (±0.005) Å and 2.745 (±0.005) Å correspondingly (Tables S4 and S5, exemplary fits in Fig. S6†). Under H_2 excess the Pd–M distances increased to 2.805 (±0.005) Å and 2.792 (±0.007) Å which are significantly shorter than in the corresponding monometallic β-PdH_x. It should be noted that absolute error bars for interatomic distances are higher than obtained from the statistics of the fits and can be up to 1%.[50] These errors stem from imperfect calculation of the theoretical scattering function by FEFF[22] and also correlation of the interatomic distances with E_0 (edge energy) which, in turn, can be defined in several ways and depends on the instrumental resolution of the beamline. Li *et al.* checked the accuracy of FEFF calculations and obtained ±0.007 Å for an Ag–Ag scattering pair (the same scattering function as Pd–Pd employed in this work).[51] On the other hand, relative bond distance variations can be observed with higher precision and the detection limit of relative shifts as low as 0.0001 Å was demonstrated by Purans *et al.* using difference EXAFS analysis.[52] In our analysis all parameters influencing interatomic distances were kept the same and, hence, we believe that the trends are accurately represented even if systematic errors mentioned above may be higher than the reported error bars.

In order to further highlight the different structure of the Pd, PdSn, and PdIn nanoparticles and since the shifts of interatomic distances are near the lower limit of EXAFS sensitivity, the trends visible in EXAFS are also supported by a direct comparison of the edge region of the Pd–K edge XANES spectra of all three catalysts under hydride-forming conditions and under O_2 (Fig. S9†). This leads to two conclusions. First, longer Pd–M distances under O_2 feed strongly suggest doping of Pd lattice by the second (larger) metal, in our case Sn and In. This conclusion is fully supported for the PdIn/s-TiO_2 catalyst by the In–K edge XANES spectra (Fig. S5†) and the In–K edge EXAFS showing the same In–M and Pd–M distances (Tables S2 and S5† and Fig. 6c and d) in the non-hydride state. Unfortunately, SnO_x species mask spectral features of reduced Sn making a similar analysis impossible for the Sn–K edge spectra. Average $Pd^0:Sn^0$ and $Pd^0:In^0$ atomic ratios under non-hydride forming conditions are 5.5 : 1 and 8.7 : 1, respectively.

Second, β-hydride formation leads to significant structure expansion of the undoped Pd lattice while expansion of the Sn- and In-doped PdSn and PdIn lattices is not so pronounced. Interestingly, whereas the average Pd–M distance in PdIn NPs increases with absorption of H (Fig. 6c), the corresponding In–M distance remains the same even in the hydride NPs (Fig. 6d). Hence, doping Pd by Sn or In limits the lattice expansion during β-hydride formation. This may be tentatively explained by a lower amount of H^- which

can be stabilized in the doped Pd lattice, possibly because H^- do not occupy interstitial sites near the dopant atoms as confirmed by the unchanged local geometry around In in the case of β-$PdInH_x$. Interestingly, Kanungo *et al.*[8] observed a similar lattice expansion in both monometallic Pd and alloyed PdAu NPs with Pd–Au distances lengthening to the same degree as Pd–Pd distances, although the formed $PdAuH_x$ hydride was less stable compared to PdH_x. This means that introducing a second metal into the Pd lattice does not always limit lattice expansion upon hydrogen uptake since a higher hydrogen solubility was also found in PdAg, PdAu, PdCu, PdCe, and PdY alloys.[53] The nature of the second metal and the doping level, structure of the alloy (random or core–shell), formation of intermetallic structures *etc.* can be decisive factors in determining the hydrogen uptake capacity and the resulting lattice expansion.

DFT calculations

To evaluate the theoretical hydrogen uptake capacity in the monometallic and bimetallic Pd lattices and confirm the structure of bimetallic PdSn and PdIn hydrides derived from *operando* EXAFS measurements, DFT calculations were performed. As a starting structure the 2 × 2 × 2 supercell containing 32 metal atoms was employed. The Pd : M ratio was set to 7 : 1, similar to the values obtained from the XAS analysis (the structures are reported in the ESI†). The hydrogen uptake of the PdM clusters was calculated and is shown in Fig. 7. It was found, that structures containing H atoms next to In or Sn dopant atoms are energetically unfavourable. Stable structures contain hydrogen atoms that are highly distributed while at the same time avoiding interstitial sites near dopant atoms. We note that the dissolution energies were calculated using the BEEF-vdW functional, while the interatomic distances were obtained using PBE-sol. In case of pure palladium, the hydrogen dissolution energy stays negative for the entire range of H : Pd ratios investigated (Fig. 7a) as also observed in earlier theoretical studies.[54] Therefore, structures with high hydrogenation degrees should be easily accessible, in practice even H : Pd ratios above 1 have been achieved.[55–57] The average Pd–Pd interatomic distance in the model with a H : Pd ratio of 0.625 was found to be very similar to the average Pd–Pd distance experimentally determined under H_2 excess (Fig. 6a and 7b).

The hydrogen dissolution energies calculated for the PdIn and PSn alloys are drastically different from those obtained for pure palladium. Investigations of the PdSn and PdIn alloys reveal that while initial hydrogen dissolution energies are similar to those of Pd, an increase in the H : (Pd + M) ratio above 1/4 (stoichiometry $H_{0.4}Pd_{(1-x)}M_x$) is prohibitively endergonic due to repulsion between hydrogen and Sn or In (Fig. 7a). As a result of the lower degree of hydrogenation, the averaged lattice expansion in the alloy hydrides is also smaller than that of the pristine Pd lattice (Fig. 7b), in agreement with the trends obtained from EXAFS analysis (Fig. 6). Hence, DFT calculations support the experimental conclusion that doping Pd with a second metal limits its lattice expansion by limiting the amount of dissolved hydrogen.

Leaching of Pd, Sn, and In during synthesis of H_2O_2

An important factor determining catalyst stability and, according to some reports,[58] also activity in the direct H_2O_2 synthesis is leaching of Pd species from the solid to the liquid phase.[59] During the reported experiments, leaching of transition metal species could be unambiguously seen from the decreased height of the absorption edge in non-normalized XANES spectra (Fig. 8a and S10†). The leaching of active species did not affect the XAS spectra, either because the amount of dissolved species was too low compared to the solid phase or because Pd(M) NPs detached from the support as a whole rather than being dissolved slowly. During the experiment no spatial gradients in the

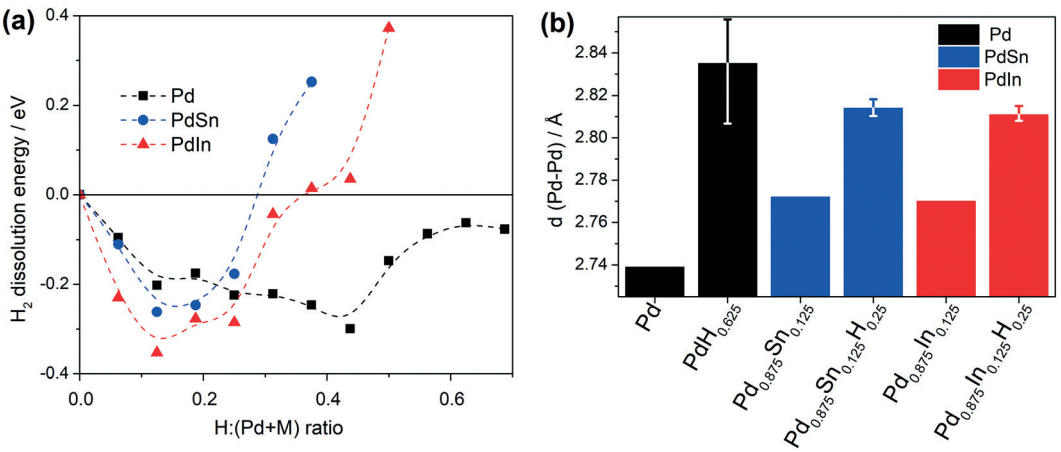

Fig. 7 (a) Calculated differential dissolution energies of hydrogen in monometallic Pd and bimetallic PdSn and PdIn lattices. Dissolution energies are calculated relative to the pure metal and H_2 in the gas-phase. (b) Calculated average Pd–M distances in the Pd, PdSn, and PdIn lattices and the corresponding hydrides. Error bars indicate the scatter of the theoretically determined bond distances.

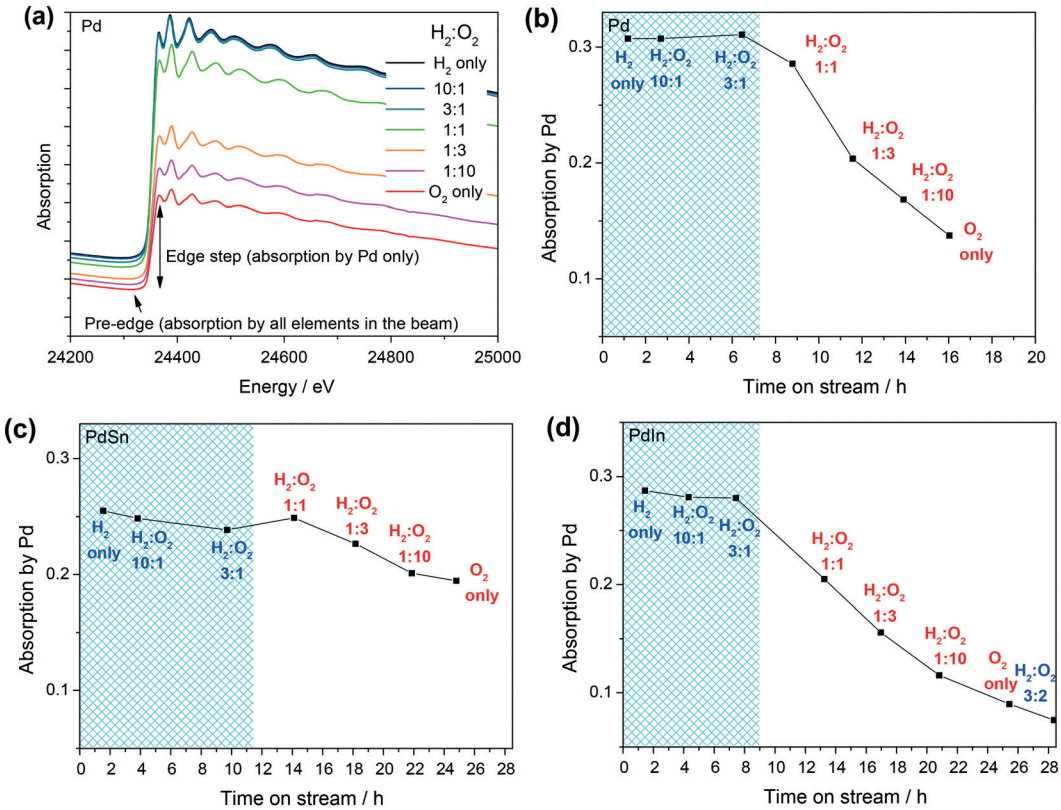

Fig. 8 (a) Decrease in the X-ray absorption as seen in the non-normalized *operando* Pd–K edge XANES spectra of the Pd/s-TiO_2 catalyst measured during H_2O_2 synthesis experiments (time-on-stream during changing conditions from H_2 only to H_2 + O_2 mixtures and, finally, to O_2 only). (b–d): Variation of X-ray absorption by Pd (inlet of the catalyst bed, corrected for absorption by X-ray windows and normalized by the total absorption of the catalyst) with time on stream and $H_2:O_2$ ratio during the direct synthesis of H_2O_2 at 80 bar over (b) Pd/s-TiO_2, (c) PdSn/s-TiO_2, and (d) PdIn/s-TiO_2. Hatch patterns designate hydride-forming conditions (H_2 excess).

concentrations of active species were found, *i.e.* the species leached out at the inlet of the catalyst bed were not trapped by the s-TiO_2 support at the outlet.

To be able to semi-quantitatively evaluate the fraction of the leached Pd species, the X-ray absorption in the pre-edge region (−30 eV from the edge position) was corrected for the amount of X-rays absorbed by the X-ray windows in the cell.[60] The Pd–K, Sn–K, and In–K edge heights were then normalized by the corrected total absorption which allows to compensate for the restructuring of the catalyst bed in the liquid flow (densification, movement of catalyst grains). The obtained values are proportional to the concentrations of the respective species in the probed volume. Fig. 8b–d shows the decrease in the corrected absorbance by Pd in the X-ray beam

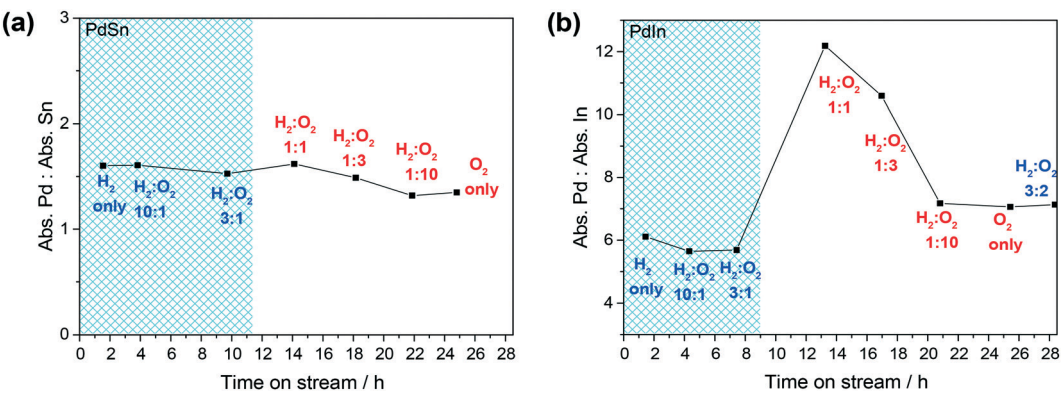

Fig. 9 Ratios of X-ray absorption by Pd to X-ray absorption by (a) Sn and (b) In (inlet of the catalyst bed, corrected for absorption by X-ray windows and normalized by the total absorption by the catalysts) with time on stream and $H_2:O_2$ ratio during the direct synthesis of H_2O_2 at 80 bar over PdSn/s-TiO_2 and PdIn/s-TiO_2. Hatch patterns designate hydride-forming conditions (H_2 excess).

during the *operando* XAS study on the Pd/s-TiO_2, PdSn/s-TiO_2, and PdIn/s-TiO_2 catalysts. Pd species in the Pd/s-TiO_2 remain stable in the solid phase under H_2 excess (all conditions under which β-PdH_x is observed), while the amount of supported Pd rapidly decreases after changing to $H_2:O_2$ ratio 1 : 1 and further to more oxidizing conditions. Within approx. 9 hours more than half of Pd was removed from the support (and also from the probed volume of the *in situ* cell).

The bimetallic PdSn/s-TiO_2 catalyst showed much higher stability. Pd species are stable under hydride-forming conditions and at a $H_2:O_2$ ratio of 1 : 1 (Fig. 8b). Even after switching to the feeds with O_2 excess, the amount of leached Pd was markedly lower than for Pd/s-TiO_2 and PdIn/s-TiO_2 with approx. 23% after 14 hours on stream. The ratio of the Pd : Sn normalized absorption edge heights was nearly constant during the whole experiment (Fig. 9a) proving that Sn species in the catalyst were also rather stable and were leached out at a similar rate to Pd species.

Unlike the PdSn/s-TiO_2, the PdIn/s-TiO_2 showed low stability in oxidizing feeds. The leaching rate of Pd species from PdIn/s-TiO_2 in the oxidizing media was high and comparable to that observed for the monometallic Pd/s-TiO_2 (Fig. 8c). Noteworthy, leaching of active species from the PdIn catalyst after switching to $H_2:O_2 = 1:1$ resulted in a very long time before the catalytic activity was stabilized and the spectra could be measured. Comparison of the relative concentrations of Pd and In (Fig. 9b) also shows that In was leached out much faster than Pd after exposure to oxidizing conditions. After switching to $H_2:O_2 = 1:1$ the Pd : In ratio was increased by two times, *i.e.* more than half of In was lost from the catalyst bed before the steady-state H_2O_2 production was observed. However, during the following hours the Pd leaching rate was faster than that of In so at the end of the experiment the Pd : In ratio was similar to that in the fresh catalyst.

Transformation and leaching of Pd species in methanol solution (excess O_2) in the presence of halide ions at ambient pressure was also observed by Centomo *et al.*[61] using *in situ* XAS. Furthermore, Pd complexes leached in the presence of halogens are generally accepted as active species of C–C coupling reactions in the basic media.[62] Our current observations, on the other hand, are made in the halogen-free acidic solution which is new, furthermore the dependence on the partial pressure of O_2 is derived. This dependence may also explain the fact that we could not previously observe Pd leaching at 10 bar in aqueous solution near stoichiometric $H_2:O_2$ ratio.[9]

Transmission electron microscopy

TEM images with particle size distributions of the as-received catalysts are reported elsewhere.[14] The corresponding images of the studied catalysts after the *operando* measurements are shown in Fig. 10. The high Pd and In leaching rates in Pd/s-TiO_2 and PdIn/s-TiO_2 resulted in only few NPs visible in the images of especially PdIn/s-TiO_2. The relative fraction of very

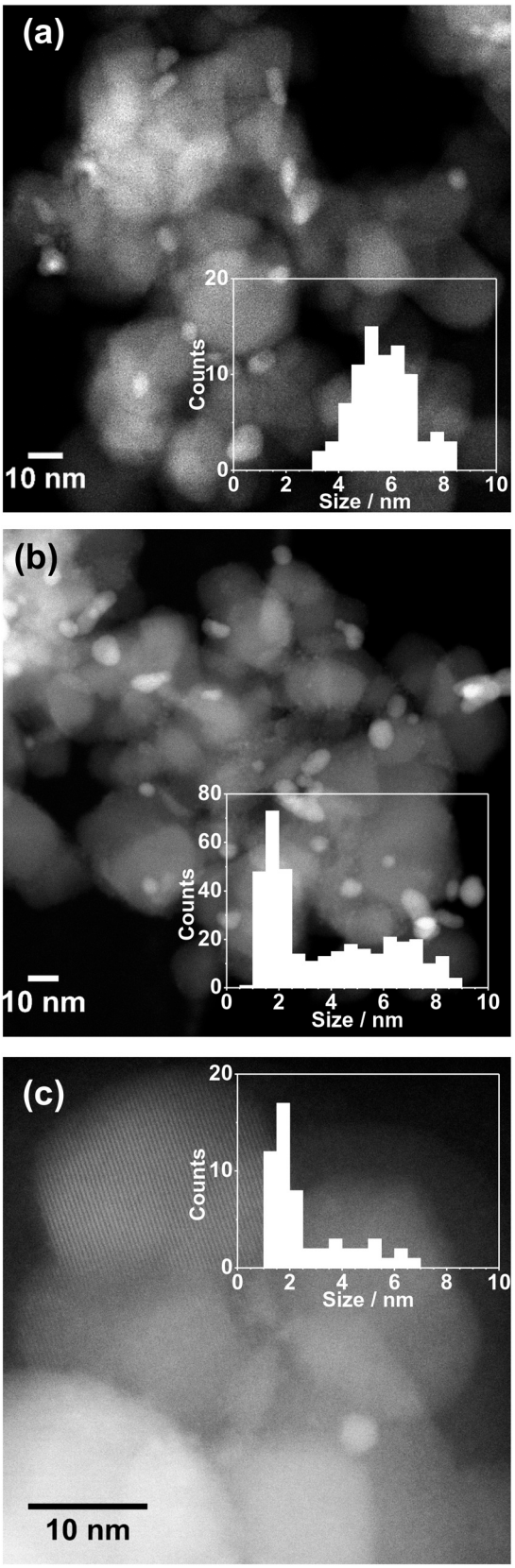

Fig. 10 STEM-HAADF images of the catalysts after *operando* XAS measurements and the corresponding particle size distributions for: (a) Pd/s-TiO_2, (b) PdSn/s-TiO_2, and (c) PdIn/s-TiO_2.

small (≤1 nm) particles/clusters did not increase after H_2O_2 synthesis experiments (compare Fig. 10a and c). Absence of very small particles and no signs of Pd–O interaction in the XAS spectra (even under the most oxidizing conditions with the highest leaching rate) lead to the suggestion that during H_2O_2 synthesis Pd(M) NPs detach from the s-TiO_2 support as a whole rather than break up or dissolve as ionic Pd^{2+} species. Weak bonding between the Pd(In) NPs and the support is probably due to the absence of calcination step during catalyst synthesis. Hence, future experiments in terms of catalyst pretreatment could further enhance the stability of these catalysts under different operating conditions.

The PdSn catalyst showed much slower leaching rate of Pd/Sn species compared to the Pd and PdIn catalysts. We relate this stabilization by Sn to the formation of a SnO_2 shell around PdSn NPs under O_2-excess conditions analogously to the observations by Freakley *et al.*[11] made after catalyst calcination. The SnO_2 layer is visible in high resolution TEM (HRTEM) images (Fig. S12a†) and may facilitate strong bonding between the s-TiO_2 support and the resulting core@shell PdSn@SnO_2 NPs, thus, hindering detachment and leaching of active species during catalysis. The synthesis of PdSn NPs and their deposition on s-TiO_2 were performed under inert conditions (see ESI† and detailed characterisation of unsupported and supported NPs in ref. 14). Hence, the SnO_2 shell must have been formed after exposure of the as-prepared supported catalyst to air. Since no thermal treatment was performed on the catalyst we exclude the possibility of the s-TiO_2 morphology change and formation of a TiO_2 shell rather than SnO_2. On the contrary, no such protective layer is formed by oxidized In species (Fig. S12b†) leading to high Pd and In leaching rates.

Discussion

In this work supported monometallic Pd and bimetallic PdSn and PdIn NPs were used as model catalysts and systematically tested in the continuous direct synthesis of H_2O_2 in the liquid phase at 80 bar and $H_2:O_2$ ratios varying from strongly reducing to strongly oxidizing conditions. The observed H_2O_2 production rates are among the highest rates compared to recent literature,[1,33] despite the employment of an *in situ* XAS cell as the reactor. Due to this compromise it could not be perfectly operated in the kinetic regime and the activity was limited by the supply of reagents (in most of the cases at nearly 100% conversion of the limiting reactant). Therefore, the already high H_2O_2 production rates could be further improved in the future, *e.g.* by substantially increasing the flow of the reaction feed. This would also allow obtaining kinetic data in future work.

Whereas previously catalysts were mostly tested in a narrow window of $H_2:O_2$ ratios with excess of O_2,[1,10–12,14] in this work the $H_2:O_2$ ratio was varied from 10 : 1 to 1 : 10 and it was found that trends in activity and stability of the catalysts strongly depend on the $H_2:O_2$ ratio (Fig. 2). For instance, under reducing conditions ($H_2:O_2$ = 3 : 1) the monometallic Pd/s-TiO_2 outperformed both alloyed catalysts producing *ca.* 4 times more H_2O_2 with a comparable selectivity. Under stoichiometric conditions the PdIn/s-TiO_2 catalyst was more active than Pd/s-TiO_2, while production of H_2O_2 over PdSn/s-TiO_2 was substantially slower. Under the most commonly tested oxidizing conditions (in our case $H_2:O_2$ = 1 : 3) otherwise not so active PdSn/s-TiO_2 showed the highest H_2O_2 yield followed by Pd/s-TiO_2 and PdIn/s-TiO_2. On the other hand, Pd/s-TiO_2 and PdIn/s-TiO_2 were not stable in oxidizing media while PdSn/s-TiO_2 demonstrated high stability under all test conditions (Fig. 8). Hence, no single catalyst formulation could cover all applications. Different catalysts are suitable for different reaction conditions, *e.g.* Pd/s-TiO_2 is active and stable under reducing conditions while PdSn/s-TiO_2 would be the catalyst of choice, both active and stable, in oxidizing media.

The improved leaching resistance of the PdSn/s-TiO_2 catalyst may be attributed to the formation of a SnO_2 shell over the PdSn NPs (Scheme 1). This model of a shell is supported by earlier results by Freakley *et al.*[11] PdIn NPs in the PdIn/s-TiO_2 catalyst did not have a similar In_2O_3 shell (Scheme 1) and showed high leaching rates in contrast to the PdSn/s-TiO_2. Hence, formation of an oxide shell over PdM NPs depends on the nature and/or concentration of the second metal and may increase the catalyst durability.

The structure of the Pd(M) NPs in all three catalysts abruptly changed between metallic and β-hydride phases depending on the $H_2:O_2$ ratio (Scheme 1). The Pd lattice expansion could be reproducibly controlled in a wide range by varying the $H_2:O_2$ ratio and the nature of the dopant metal. The monometallic Pd/s-TiO_2 showed high activity in both hydride and metallic states (the highest and the lowest observed Pd–Pd distances) while PdSn and PdIn were not

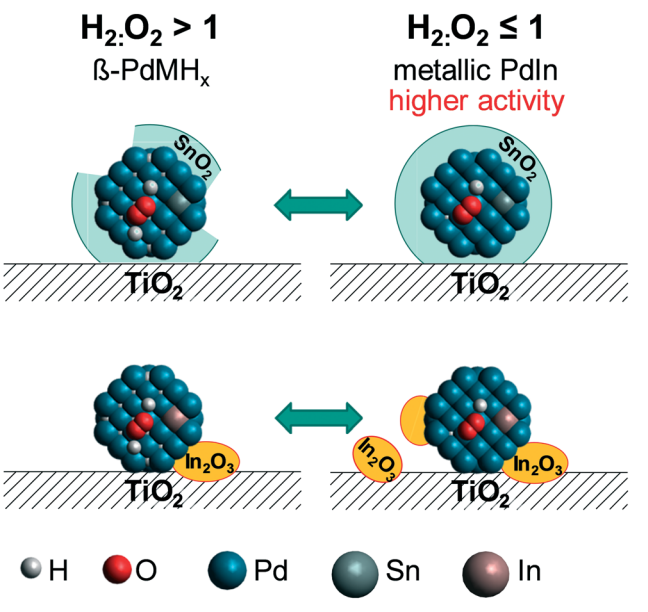

Scheme 1 Schematic representation of transformations of PdSn and PdIn NPs in the reaction feed with different $H_2:O_2$ ratios.

active in the hydride state despite having intermediate Pd–Pd(M) distances (Fig. 6). Moreover, Pd–Pd(M) distances in PdSn and PdIn catalysts were similar but the activity was different, *e.g.* at $H_2:O_2 = 1:1$. The observations rule out a direct dependence of activity and selectivity of Pd(M) catalysts on the Pd–Pd bond length and/or PdH_x formation in the tested catalysts. Instead, the chemical nature of the dopant which changes electronic structure of Pd species may play a role in the direct H_2O_2 synthesis.

The observed structure–activity correlations rule out leached species as active sites for H_2O_2 direct synthesis because Pd/s-TiO_2 demonstrated high activity and PdIn/s-TiO_2 – considerable activity also under hydride-forming conditions. Under reducing conditions the catalysts were very stable and no leaching could be observed. This conclusion is also in agreement with our previous *operando* study of the direct synthesis of H_2O_2.[9] On the other hand, both bimetallic catalysts showed high activity only at $H_2:O_2 \leq 1$ which we tentatively attribute to partial leaching of the second metal oxide species which results in reconstruction of the shell around metallic PdM NPs and provides access of the reactants to the Pd surface. This effect, although very small, is especially important for the PdSn/s-TiO_2 in which >70% Sn forms oxide even under net reducing conditions blocking access to the Pd surface. As a result of very slow leaching of Pd and Sn species the PdSn/s-TiO_2 displays high activity only under O_2 excess, long after the first leaching inducing conditions were applied.

Conclusions

The used *in situ* setup for direct hydrogen peroxide synthesis provided both realistic catalytic data with H_2O_2 production rates close to the highest reported in literature and structural analysis by *operando* XANES and EXAFS. The highest obtained H_2O_2 concentration was 80 mmol L^{-1} (approx. 0.3 wt%) over the bimetallic PdIn/s-TiO_2 catalyst, corresponding to a productivity of 579 $mmol_{H_2O_2}\ g_{cat}^{-1}\ h^{-1}$.

Along the wide range of $H_2:O_2$ ratios a strong influence of reaction conditions on hydride formation in Pd, PdIn, and PdSn-based catalysts was found. The observed hydrogen uptake could be supported by theoretical calculations. Doping Pd NPs with a second metal limited hydrogen uptake to a stoichiometry of $H_{0.4}Pd_{(1-x)}M_x$. Also the leaching could be directly observed by XAS, demonstrating stabilization by Sn (Scheme 1).

Conflicts of interest

There are no conflicts to declare.

Acknowledgements

Funding was provided by the Helmholtz Association within the program Science and Technology of Nanosystems (STN). We thank Susanne Eissler (IMVT) for help during synchrotron measurements, H_2O_2 titration with $Ce(SO_4)_2$, and help with data evaluation. We would like to thank the Institute for Beam Physics and Technology (IBPT) for the operation of the storage ring, the Karlsruhe Research Accelerator (KARA). We acknowledge Dr. Tim Prüßmann for his help and technical support during experiments. TEM measurements were carried out with the support of the Karlsruhe Nano Micro Facility (KNMF), a Helmholtz Research Infrastructure at Karlsruhe Institute of Technology (KIT). We also thank Petra Janke (IKFT) for the Karl Fischer titration. The authors acknowledge support by the state of Baden-Württemberg through bwHPC (bwunicluster and JUSTUS, RV bw17D011). The authors would like to acknowledge the VirtMat project. BJD and RD acknowledge funding of this work by the German Research Foundation DFG through the Research Unit 2383 "ProMiSe" (www.promise.kit.edu) under grant numbers Di 696/13-1 and Di 696/14-1.

References

1 J. K. Edwards, S. J. Freakley, R. J. Lewis, J. C. Pritchard and G. J. Hutchings, Advances in the direct synthesis of hydrogen peroxide from hydrogen and oxygen, *Catal. Today*, 2015, **248**, 3–9.
2 D. W. Flaherty, Direct Synthesis of H_2O_2 from H_2 and O_2 on Pd Catalysts: Current Understanding, Outstanding Questions, and Research Needs, *ACS Catal.*, 2018, **8**, 1520–1527.
3 S. Yang, A. Verdaguer-Casadevall, L. Arnarson, L. Silvioli, V. Čolić, R. Frydendal, J. Rossmeisl, I. Chorkendorff and I. E. L. Stephens, Toward the Decentralized Electrochemical Production of H_2O_2: A Focus on the Catalysis, *ACS Catal.*, 2018, **8**, 4064–4081.
4 R. Ciriminna, L. Albanese, F. Meneguzzo and M. Pagliaro, Hydrogen Peroxide: A Key Chemical for Today's Sustainable Development, *ChemSusChem*, 2016, **9**, 3374–3381.
5 H.-J. Riedl and G. Pfleiderer, Production of hydrogen peroxide, *US Pat.*, US2158525A, 1939.
6 R. Dittmeyer, J.-D. Grunwaldt and A. Pashkova, A review of catalyst performance and novel reaction engineering concepts in direct synthesis of hydrogen peroxide, *Catal. Today*, 2015, **248**, 149–159.
7 M. Selinsek, M. Kraut and R. Dittmeyer, Experimental Evaluation of a Membrane Micro Channel Reactor for Liquid Phase Direct Synthesis of Hydrogen Peroxide in Continuous Flow Using Nafion® Membranes for Safe Utilization of Undiluted Reactants, *Catalysts*, 2018, **8**, 556.
8 S. Kanungo, L. van Haandel, E. J. M. Hensen, J. C. Schouten and M. F. Neira d'Angelo, Direct synthesis of H_2O_2 in AuPd coated micro channels: An in-situ X-Ray absorption spectroscopic study, *J. Catal.*, 2019, **370**, 200–209.
9 M. Selinsek, B. J. Deschner, D. E. Doronkin, T. L. Sheppard, J.-D. Grunwaldt and R. Dittmeyer, Revealing the Structure and Mechanism of Palladium during Direct Synthesis of Hydrogen Peroxide in Continuous Flow Using Operando Spectroscopy, *ACS Catal.*, 2018, **8**, 2546–2557.
10 N. M. Wilson, P. Priyadarshini, S. Kunz and D. W. Flaherty, Direct synthesis of H_2O_2 on Pd and Au_xPd_1 clusters: Understanding the effects of alloying Pd with Au, *J. Catal.*, 2018, **357**, 163–175.

11 S. J. Freakley, Q. He, J. H. Harrhy, L. Lu, D. A. Crole, D. J. Morgan, E. N. Ntainjua, J. K. Edwards, A. F. Carley, A. Y. Borisevich, C. J. Kiely and G. J. Hutchings, Palladium-tin catalysts for the direct synthesis of H_2O_2 with high selectivity, *Science*, 2016, **351**, 965–968.

12 S. Kanungo, V. Paunovic, J. C. Schouten and M. F. Neira D'Angelo, Facile Synthesis of Catalytic AuPd Nanoparticles within Capillary Microreactors Using Polyelectrolyte Multilayers for the Direct Synthesis of H_2O_2, *Nano Lett.*, 2017, **17**, 6481–6486.

13 S. Wang, R. J. Lewis, D. E. Doronkin, D. J. Morgan, J.-D. Grunwaldt, G. J. Hutchings and S. Behrens, The direct synthesis of hydrogen peroxide from H_2 and O_2 using Pd–Ga and Pd–In catalysts, *Catal. Sci. Technol.*, 2020, **10**, 1925–1932.

14 S. Wang, D. E. Doronkin, M. Hähsler, X. Huang, D. Wang, J.-D. Grunwaldt and S. Behrens, Pd-Based Bimetallic Nanocrystal Catalysts for the Direct Synthesis of H_2O_2, *ChemSusChem*, 2020, **13**, 3243–3251.

15 *HH-056 H_2O_2 Passivation Procedure*, Solvay Chemicals, 2005, accessed 19.03.2020, https://www.solvay.us/en/binaries/HH-056_Passivation-236794.pdf.

16 D. P. Nolan, in *Handbook of Fire and Explosion Protection Engineering Principles for Oil, Gas, Chemical, and Related Facilities*, Gulf Professional Publishing, Elsevier, Cambridge, MA, United States, Kidlington, Oxford, United Kingdom, 2019, pp. 279–302.

17 A. Pashkova, K. Svajda, G. Black and R. Dittmeyer, Automated system for spectrophotometric detection of liquid phase hydrogen peroxide for concentrations up to 5% w/w, *Rev. Sci. Instrum.*, 2009, **80**, 055104.

18 G. Czapski, B. H. J. Bielski and N. Sutin, The Kinetics of the Oxidation of Hydrogen Peroxide by Cerium(IV), *J. Phys. Chem.*, 1963, **67**, 201–203.

19 K. Fischer, Neues Verfahren zur maßanalytischen Bestimmung des Wassergehaltes von Flüssigkeiten und festen Körpern, *Angew. Chem., Int. Ed. Engl.*, 1935, **48**, 394–396.

20 A. Zimina, K. Dardenne, M. A. Denecke, D. E. Doronkin, E. Huttel, H. Lichtenberg, S. Mangold, T. Pruessmann, J. Rothe, T. Spangenberg, R. Steininger, T. Vitova, H. Geckeis and J.-D. Grunwaldt, CAT-ACT – a new highly versatile X-ray spectroscopy beamline for catalysis and radionuclide science at the KIT synchrotron light facility ANKA, *Rev. Sci. Instrum.*, 2017, **88**, 113113.

21 B. Ravel and M. Newville, ATHENA, ARTEMIS, HEPHAESTUS: data analysis for X-ray absorption spectroscopy using IFEFFIT, *J. Synchrotron Radiat.*, 2005, **12**, 537–541.

22 J. J. Rehr and R. C. Albers, Theoretical approaches to x-ray absorption fine structure, *Rev. Mod. Phys.*, 2000, **72**, 621–654.

23 G. Kresse and J. Furthmüller, Efficient iterative schemes for ab initio total-energy calculations using a plane-wave basis set, *Phys. Rev. B: Condens. Matter Mater. Phys.*, 1996, **54**, 11169–11186.

24 A. E. Mattsson, R. Armiento, J. Paier, G. Kresse, J. M. Wills and T. R. Mattsson, The AM05 density functional applied to solids, *J. Chem. Phys.*, 2008, **128**, 084714.

25 J. Wellendorff, K. T. Lundgaard, A. Møgelhøj, V. Petzold, D. D. Landis, J. K. Nørskov, T. Bligaard and K. W. Jacobsen, Density functionals for surface science: Exchange-correlation model development with Bayesian error estimation, *Phys. Rev. B: Condens. Matter Mater. Phys.*, 2012, **85**, 235149.

26 J. Wellendorff, T. L. Silbaugh, D. Garcia-Pintos, J. K. Nørskov, T. Bligaard, F. Studt and C. T. Campbell, A benchmark database for adsorption bond energies to transition metal surfaces and comparison to selected DFT functionals, *Surf. Sci.*, 2015, **640**, 36–44.

27 S. Mallikarjun Sharada, T. Bligaard, A. C. Luntz, G.-J. Kroes and J. K. Nørskov, SBH10: A Benchmark Database of Barrier Heights on Transition Metal Surfaces, *J. Phys. Chem. C*, 2017, **121**, 19807–19815.

28 J. P. Perdew, A. Ruzsinszky, G. I. Csonka, O. A. Vydrov, G. E. Scuseria, L. A. Constantin, X. Zhou and K. Burke, Restoring the Density-Gradient Expansion for Exchange in Solids and Surfaces, *Phys. Rev. Lett.*, 2008, **100**, 136406.

29 J. R. Knight and D. W. Rhys, The systems palladium - indium and palladium - tin, *J. Less-Common Met.*, 1959, **1**, 292–303.

30 Y. Sakamoto, E. Kakihisa and Y. Kinari, Absorption of Hydrogen by Pd-Al and Pd-In Solid Solution Alloys, *Z. Phys. Chem.*, 1993, **179**, 69–75.

31 H. Okamoto, Pd-Sn (Palladium-Tin), *J. Phase Equilib. Diffus.*, 2012, **33**, 253–254.

32 C. A. Schneider, W. S. Rasband and K. W. Eliceiri, NIH Image to ImageJ: 25 years of image analysis, *Nat. Methods*, 2012, **9**, 671–675.

33 D. Gudarzi, W. Ratchananusorn, I. Turunen, M. Heinonen and T. Salmi, Promotional effects of Au in Pd–Au bimetallic catalysts supported on activated carbon cloth (ACC) for direct synthesis of H_2O_2 from H_2 and O_2, *Catal. Today*, 2015, **248**, 58–68.

34 J.-D. Grunwaldt, M. Caravati and A. Baiker, Oxidic or Metallic Palladium: Which Is the Active Phase in Pd-Catalyzed Aerobic Alcohol Oxidation?, *J. Phys. Chem. B*, 2006, **110**, 25586–25589.

35 B. J. Deschner, D. E. Doronkin, T. L. Sheppard, A. Zimina, J.-D. Grunwaldt and R. Dittmeyer, The Effect of Selectivity Enhancers on the Structure of Palladium during High-Pressure Continuous-Flow Direct Synthesis of Hydrogen Peroxide in Ethanol, unpublished work.

36 A. Jentys, Estimation of mean size and shape of small metal particles by EXAFS, *Phys. Chem. Chem. Phys.*, 1999, **1**, 4059–4063.

37 P. Nolte, A. Stierle, N. Kasper, N. Y. Jin-Phillipp, H. Reichert, A. Rühm, J. Okasinski, H. Dosch and S. Schöder, Combinatorial high-energy x-ray microbeam study of the size-dependent oxidation of Pd nanoparticles on MgO(100), *Phys. Rev. B: Condens. Matter Mater. Phys.*, 2008, **77**, 115444.

38 T. Schalow, B. Brandt, D. E. Starr, M. Laurin, S. K. Shaikhutdinov, S. Schauermann, J. Libuda and H.-J. Freund, Size-Dependent Oxidation Mechanism of Supported Pd Nanoparticles, *Angew. Chem., Int. Ed.*, 2006, **45**, 3693–3697.

39 S. Zhao, Y. Li, D. Liu, J. Liu, Y.-M. Liu, D. N. Zakharov, Q. Wu, A. Orlov, A. A. Gewirth, E. A. Stach, R. G. Nuzzo and A. I. Frenkel, Multimodal Study of the Speciations and

Activities of Supported Pd Catalysts During the Hydrogenation of Ethylene, *J. Phys. Chem. C*, 2017, **121**, 18962–18972.

40 A. L. Bugaev, A. A. Guda, K. A. Lomachenko, V. V. Srabionyan, L. A. Bugaev, A. V. Soldatov, C. Lamberti, V. P. Dmitriev and J. A. van Bokhoven, Temperature- and Pressure-Dependent Hydrogen Concentration in Supported PdH_x Nanoparticles by Pd K-Edge X-ray Absorption Spectroscopy, *J. Phys. Chem. C*, 2014, **118**, 10416–10423.

41 S. N. Reifsnyder and H. H. Lamb, Pd/silica cluster catalysts: synthesis and reactivity with H_2 and C_2H_4, *Catal. Lett.*, 1996, **40**, 155–161.

42 M. Suleiman, N. M. Jisrawi, O. Dankert, M. T. Reetz, C. Bähtz, R. Kirchheim and A. Pundt, Phase transition and lattice expansion during hydrogen loading of nanometer sized palladium clusters, *J. Alloys Compd.*, 2003, **356–357**, 644–648.

43 R. J. Davis, S. M. Landry, J. A. Horsley and M. Boudart, X-ray-absorption study of the interaction of hydrogen with clusters of supported palladium, *Phys. Rev. B: Condens. Matter Mater. Phys.*, 1989, **39**, 10580–10583.

44 C. Keresszegi, J.-D. Grunwaldt, T. Mallat and A. Baiker, In situ EXAFS study on the oxidation state of Pd/Al_2O_3 and $Bi–Pd/Al_2O_3$ during the liquid-phase oxidation of 1-phenylethanol, *J. Catal.*, 2004, **222**, 268–280.

45 C. Zlotea, F. Cuevas, V. Paul-Boncour, E. Leroy, P. Dibandjo, R. Gadiou, C. Vix-Guterl and M. Latroche, Size-Dependent Hydrogen Sorption in Ultrasmall Pd Clusters Embedded in a Mesoporous Carbon Template, *J. Am. Chem. Soc.*, 2010, **132**, 7720–7729.

46 A. Rose, S. Maniguet, R. J. Mathew, C. Slater, J. Yao and A. E. Russell, Hydride phase formation in carbon supported palladium nanoparticle electrodes investigated using in situ EXAFS and XRD, *Phys. Chem. Chem. Phys.*, 2003, **5**, 3220–3225.

47 Z. Karpiński, Catalysis by Supported, Unsupported, and Electron-Deficient Palladium, *Adv. Catal.*, 1990, **37**, 45–100.

48 Y. Song, H. Modrow, L. L. Henry, C. K. Saw, E. E. Doomes, V. Palshin, J. Hormes and C. S. S. R. Kumar, Microfluidic Synthesis of Cobalt Nanoparticles, *Chem. Mater.*, 2006, **18**, 2817–2827.

49 P. C. Angelomé, L. Andrini, M. E. Calvo, F. G. Requejo, S. A. Bilmes and G. J. A. A. Soler-Illia, Mesoporous Anatase TiO_2 Films: Use of Ti K XANES for the Quantification of the Nanocrystalline Character and Substrate Effects in the Photocatalysis Behavior, *J. Phys. Chem. C*, 2007, **111**, 10886–10893.

50 D. C. Koningsberger, B. L. Mojet, G. E. van Dorssen and D. E. Ramaker, XAFS spectroscopy; fundamental principles and data analysis, *Top. Catal.*, 2000, **10**, 143–155.

51 G. G. Li, F. Bridges and C. H. Booth, X-ray-absorption fine-structure standards: A comparison of experiment and theory, *Phys. Rev. B: Condens. Matter Mater. Phys.*, 1995, **52**, 6332–6348.

52 J. Purans, N. D. Afify, G. Dalba, R. Grisenti, S. De Panfilis, A. Kuzmin, V. I. Ozhogin, F. Rocca, A. Sanson, S. I. Tiutiunnikov and P. Fornasini, Isotopic Effect In Extended X-Ray-Absorption Fine Structure of Germanium, *Phys. Rev. Lett.*, 2008, **100**, 055901.

53 A. G. Knapton, Palladium Alloys for Hydrogen Diffusion Membranes, *Platinum Met. Rev.*, 1977, **21**, 44–50.

54 F. Studt, F. Abild-Pedersen, T. Bligaard, R. Z. Sørensen, C. H. Christensen and J. K. Nørskov, On the Role of Surface Modifications of Palladium Catalysts in the Selective Hydrogenation of Acetylene, *Angew. Chem., Int. Ed.*, 2008, **47**, 9299–9302.

55 J. E. Schirber and B. Morosin, Lattice constants of $\beta - PdH_x$ and $\beta - PdD_x$ with x near 1.0, *Phys. Rev. B*, 1975, **12**, 117–118.

56 R. V. Baranova, Yu. P. Khodyrev, R. M. Imamov and S. A. Semiletov, The crystal structure of palladium hydryde with primitive cubic lattice (a = 2.995a), *Kristallografiya*, 1980, **25**, 1290–1291.

57 S. A. Semiletov, R. V. Baranova, Yu. P. Khodyrev and R. M. Imamov, The electron-diffraction investigation of tetragonal $PdH_{1.3}$, *Kristallografiya*, 1980, **25**, 1162–1168.

58 D. P. Dissanayake and J. H. Lunsford, Evidence for the Role of Colloidal Palladium in the Catalytic Formation of H_2O_2 from H_2 and O_2, *J. Catal.*, 2002, **206**, 173–176.

59 G. Gallina, J. García-Serna, T. O. Salmi, P. Canu and P. Biasi, Bromide and Acids: A Comprehensive Study on Their Role on the Hydrogen Peroxide Direct Synthesis, *Ind. Eng. Chem. Res.*, 2017, **56**, 13367–13378.

60 B. L. Henke, E. M. Gullikson and J. C. Davis, X-Ray Interactions: Photoabsorption, Scattering, Transmission, and Reflection at E = 50-30,000 eV, Z = 1-92, *At. Data Nucl. Data Tables*, 1993, **54**, 181–342.

61 P. Centomo, C. Meneghini, S. Sterchele, A. Trapananti, G. Aquilanti and M. Zecca, In Situ X-ray Absorption Fine Structure Spectroscopy of a Palladium Catalyst for the Direct Synthesis of Hydrogen Peroxide: Leaching and Reduction of the Metal Phase in the Presence of Bromide Ions, *ChemCatChem*, 2015, **7**, 3712–3718.

62 D. Astruc, Palladium Nanoparticles as Efficient Green Homogeneous and Heterogeneous Carbon–Carbon Coupling Precatalysts: A Unifying View, *Inorg. Chem.*, 2007, **46**, 1884–1894.